Supporting Appendix

Nanosecond ALEX (nsALEX)

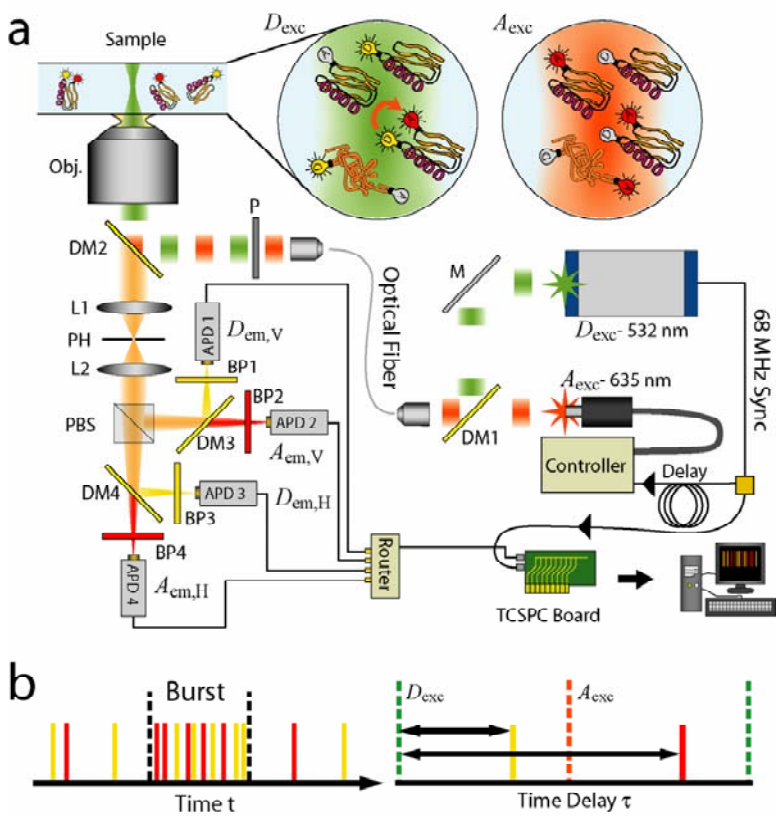

Fig. 6. a. Experimental setup used for ns-ALEX. Two picosecond pulsed lasers D_{exc} (IC-532-1000 ps Nd:VAN, High Q Laser Production GmbH) and A_{exc} (LDH 635-B, PicoQuant GmbH) are synchronized, with a fixed delay between pulses. The excitation light from D_{exc} and A_{exc} is combined by dichroic mirror (DM) DM1 (550DRLP, Omega Optical) and coupled into an optical fiber. The excitation light is coupled out of the fiber, collimated, polarized by a polarizer set to vertical (V) or horizontal (H), reflected by DM2 (400-535-635TBDR, Omega Optical), and focused by the microscope objective (Zeiss 100X Apochromat, NA 1.4) into the sample. Any fluorescence or scattered photons from the sample are collected by the same objective. After the D_{exc} pulse (green disk), only *D* and FRET sensitized *A* emission photons are collected. After the A_{exc} pulse (red disk), only *A* emission photons are collected. Collected photons then pass through DM2, focused by the tube lens (L1) onto the pinhole (PH; used to eliminate out-of-focus light), and refocused by lens L2. The collected photons are then split by a polarizing beam splitter (PBS) into vertical (V) and horizontal (H) polarizations, and split again by DM3 and DM4 (630DRLP, Omega Optical) into *D* and *A* emissions. Bandpass filters BP1-BP4 (BP1&3: 580DF30; BP2&4: 661AGLP, Omega Optical) exclude photons of the incorrect wavelength. The signals are detected by avalanche photodiodes APD1-APD4 (SPCM-AQR-14, PerkinElmer), forming the detection channels $D_{em,V}$, $A_{em,V}$, $D_{em,H}$, and $A_{em,H}$. Each detected photon produces an electronic pulse which passes through the router (which allows multiple channels to be timed using the same TCSPC board; SPC-630, Becker and Hickl GmBH), and is timed using the TCSPC plug-in board ('microtiming'). The resulting data are stored in a computer. **b**. Detected photons are also timed with 50 ns resolution ('macrotiming'), and classified by spectrum (*D* (yellow) or *A* (red)) and polarization (left panel). Photons delimited by dotted lines show an example photon burst from a single molecule diffusing through laser spot. Interlacing pulses from two lasers (right panel), D_{exc} (green; excites *D*) and A_{exc} (red; excites *A*), with

a fixed delay provides a 14.7 ns alternation period for nsALEX. The time delay between the detected photons and the D_{exc} laser pulse is measured with 17 ps nominal resolution; the actual resolution of ~500 ps depends on laser pulse width and the APD time resolution. The time delay provides fluorescence lifetime and the ability to classify photons as due to D_{exc} or A_{exc} (whether time delay τ is before or after the A_{exc} pulse).

For each photon burst in nsALEX, we count $F^{D_{em}}$, the number of *D* photons, $F_{D_{exc}}^{A_{em}}$, the number of *A* photons excited by D_{exc}, and $F_{A_{exc}}^{A_{em}}$, the number of *A* photons excited by A_{exc}. The distance-dependent energy transfer efficiency ratio *E* is

$$E = F_{D_{exc}}^{A_{em}} \Big/ \left(F_{D_{exc}}^{A_{em}} + F^{D_{em}} \right), \tag{1}$$

The *A* emission due to FRET is separated from the *A* emission due to A_{exc} laser; hence, we calculate the ALEX-specific stoichiometric ratio *S*,

$$S = \left(F^{D_{em}} + F_{D_{exc}}^{A_{em}} \right) \Big/ \left(F^{D_{em}} + F_{D_{exc}}^{A_{em}} + F_{A_{exc}}^{A_{em}} \right) \tag{2}$$

S affords molecular sorting into a *D*-only sub-population, an *A*-only sub-population, and a sub-population containing both *D* and *A* on the same chain (or two interacting chains). This sub-population can be further sorted according to *E*. Distance distributions that fluctuate slower than the photon burst durations are distinguished in two-dimensional (2D) E-S histograms as "static" species with different values of *E* and *S* (figure 2a). Since we use the burst analysis only to sort molecules into different species, differences in detection and quantum efficiencies of *D* and *A*, direct excitation of *A* by D_{exc}, and leakage of *D* into $A_{em,V}$ and $A_{em,H}$ are ignored in this expression. Ignoring these corrections does not affect the resolving power of the method.

Accuracy of Subpopulation Analysis

As explained in the previous section, we accumulate photons from individual subpopulations, and perform lifetime analysis on those photons. This section discusses what fraction of photons in a histogram come from the selected subpopulation.

Simple Background Subtraction. We obtain the background lifetime histograms in the burst analysis by forming the lifetime histograms for all of the photons *not* in bursts. The correction for $y_{sel}^{D_{em,V}}(\tau)$ is calculated (normalized by duration),

$$\Delta_{sel}^{D_{em,V}}(\tau) = y_{non\text{-}burst}^{D_{em,V}}(\tau) \left(\text{Total selected burst time} \right) \Big/ \left(\text{Total non-burst time} \right) \tag{3}$$

An example of background subtraction is shown in figure 7; only Fit 3, which uses equation (3), accounts for the background well.

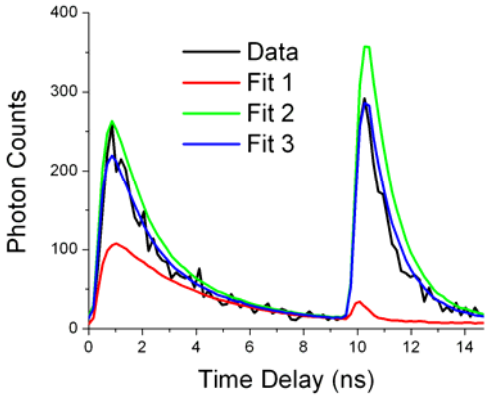

Fig. 7. Data is from the parallel *A* channel of the *D*-only subpopulation for a sample also containing a D-A labeled subpopulation exhibiting high *E*. The acceptor signal seen in the *D*-only subpopulation is due to photons from the *D-A* subpopulation that "leak" into the selected subpopulation. The decay to the left is for the D_{exc} pulse, and has contributions from leakage of *D* into the *A* channel, background scattering, and FRET photons that leaked in from *D-A* labeled molecules. The decay to the right is for the A_{exc} pulse, and has contributions from background scattering and photons that leaked in from *D-A* labeled molecules. All three fits account for the leakage of *D* into the *A* channel using a fixed fraction (determined at high concentration) of the fitted curve in the *D* channel. Fit 1 accounts for additional background photons using an averaged histogram from a separate, buffer-only sample. Fit 2 accounts for additional background photons using an averaged histogram for the entire data file for the sample. Fit 3 accounts for background photons using an averaged histogram for all of the photons in the file **not** in bursts.

Accuracy of Photon Selection. We use simulations of fluorescent molecules diffusing through a tightly focused laser excitation volume to determine the accuracy of our background subtraction method. The basic diffusion simulation procedure has been described previously(1). Here, we simulate samples containing three species with varying ratios of intensities in three channels: *D* (donor channel), $A_{D_{exc}}$ (acceptor channel excited by D_{exc}), $A_{A_{exc}}$ (acceptor channel excited by A_{exc}). Burst searches are performed as for the experimental data(2), and bursts are sorted by *E* and *S*.

In these simulations, each photon is tagged with the species that emitted the photon. For each selected subpopulation, we form a histogram of the number of photons detected from each species. The background subtraction procedure described above is performed on these data sets, and the accuracy of this correction is determined.

We first performed three-species simulations with background, with an average molecular occupancy of 0.05 of each species inside the confocal detection volume. The background count rates were 1 kHz in *D*, 1.0 kHz in $A_{D_{exc}}$, and 0.0 kHz in $A_{A_{exc}}$. We found that inside the bursts, the background count rates

range from 1.0 to 1.2 kHz. After the correction from equation (3), the remaining background count rates range from 0.0 to 0.2 kHz. The fraction of photons coming from the selected species is above 95%, except in cases where the selected peak lies between two other subpopulations. This situation is illustrated in figure 8a. The positions of bursts for each of the three species are shown as circles (1, 2, and 3). Multi-molecular bursts resulting from molecules of species 1 and 3 crossing the confocal volume at the same time lead to bursts with intermediate *E* and *S* (shown in red). These bursts are often classified as belonging to species 2, contaminating the histograms for species 2. In our experimental data, this issue is important for studying the lifetime histograms of the unfolded protein states (especially for CI2; figures 8b-c).

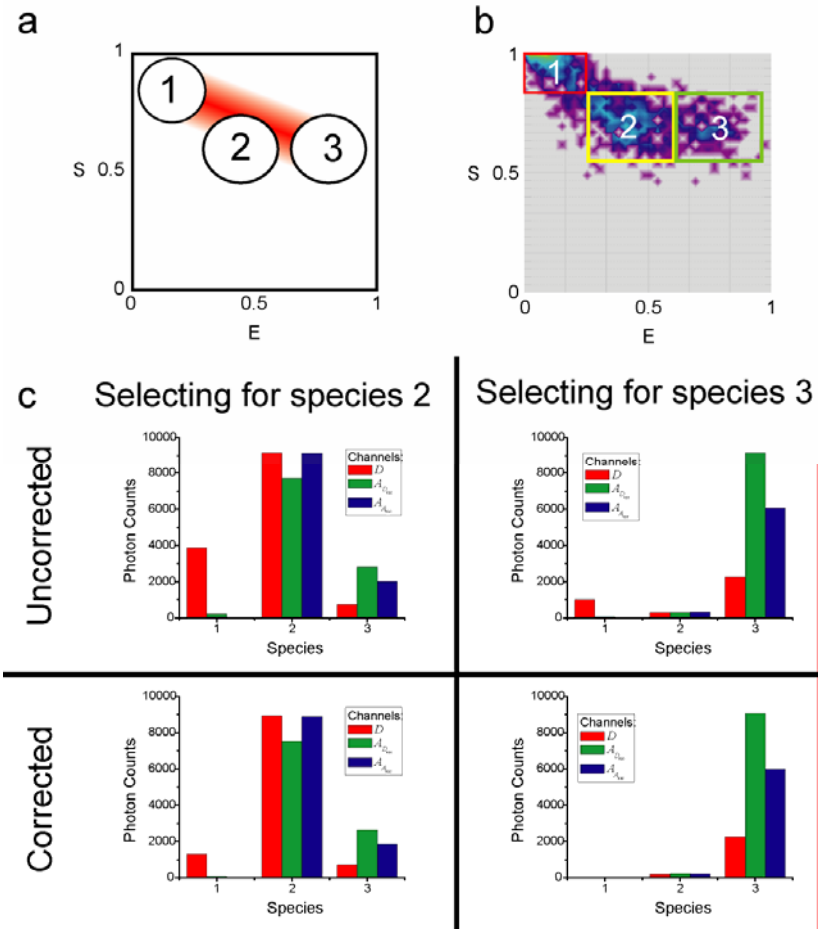

Fig. 8. a. Schematic of *E-S* histogram of bursts for a sample containing three species. Bursts from species 2 lie in between species 1 and 3. Bursts resulting from molecules of species 1 and 3 crossing the confocal detection volume simultaneously also lie in between species 1 and 3 (shown in red). Such multi-molecular events allow photons from species 1 and 3 to be mis-classified as coming from species 2. **b**. *E-S* histogram for a simulation designed to match the conditions for a sample containing the CI2 labeled at positions 1 and 53, with 4 M GdnCl added. Species 1 simulates contaminants in the GdnCl and CI2 with only *D* attached. Species 2 simulates the unfolded CI2, and species 3 simulates the folded CI2. The selection regions for species 1, 2, and 3 correspond to the red, yellow, and green squares, respectively. **c**. The number of photons from each species classified as coming from species 2 and 3 for each channel. Due to the multi-

molecular events, the leakage of species 1 and species 3 photons into the selection for species 2 is significant, even after background subtraction, and therefore needs to be corrected. However, the leakage in photons classified as species 1 and species 2 into the selection for species 3 is insignificant after the background subtraction.

For the unfolded species of CI2, we use these simulations to correct for the leakage of photons from folded CI2 and *D*-only CI2. The lifetime curves for species with *D*-only and the folded species are obtained accurately using burst selection. Simulations are created that match the experimental conditions, finding fractions of the number of photons attributed to the unfolded species which are really from the folded and *D*-only species. Fits for the experiments involving the unfolded species take these fractions into account, and allow accurate extraction of the unfolded species properties. The lifetime curves for the *D*-only ($y_{\text{D-only}}^{D_{\text{em,V}}}(\tau)$, etc.) and folded ($y_{\text{folded}}^{D_{\text{em,V}}}(\tau)$, etc.) subpopulations are fitted separately. Fits for lifetime curves of the unfolded subpopulation account for leakage of these subpopulations, $y_{\text{unfolded}}^{D_{\text{em,V}}}(\tau) = y_{\text{pure unfolded}}^{D_{\text{em,V}}}(\tau) + c_1 y_{\text{D-only}}^{D_{\text{em,V}}}(\tau) + c_2 y_{\text{folded}}^{D_{\text{em,V}}}(\tau)$; the total measured lifetime curve $y_{\text{unfolded}}^{D_{\text{em,V}}}(\tau)$ has contributions from the "pure" unfolded lifetime curve and from the *D*-only and folded subpopulations (similar equations are used for each detection channel). The constants c_1 and c_2 are determined from the simulations described above. For each detection channel, this procedure was applied to the data taken for the CI2 labeled at positions 1 and 53 when both folded and unfolded species are present (figure 3).

“Phase Diagram” for Polymer Fluctuations

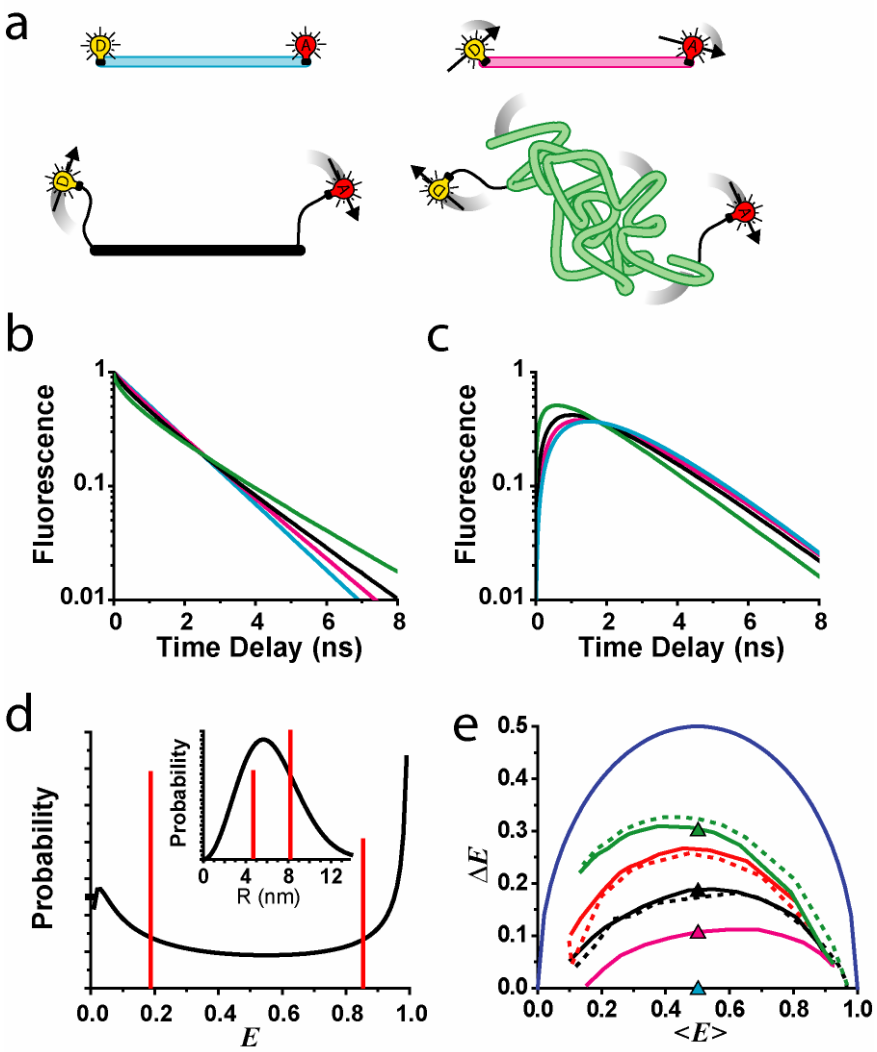

Fig. 9. Extraction of FRET efficiency *E* and polymer distance distributions using TR-FRET. **a.** Four polymers and fluorophore rotational diffusion regimes. **Cyan:** a rigid rod with fast fluorophore rotation leading to $\langle\kappa^2\rangle = 2/3$ ($\tau_r \ll \tau_f$). **Magenta:** a rigid rod with slow rotational diffusion resulting in κ^2 fluctuations ($\langle\kappa^2\rangle < 2/3$; $\tau_r \approx \tau_f$). **Black**: a rigid rod polymer where rotating fluorophores are attached via flexible linkers. **Green:** Gaussian-chain model where rotating fluorophores are linked via flexible linkers. **b**. Corresponding donor (*D*) fluorescence lifetime curves (colors as in **a.**). The parameters used are from dsDNA and ssDNA: $R_0 = 6.9$ nm, $\tau_{f,0}^D = 3.1$ ns, and $\tau_f^A = 1.6$ ns. When $\tau_r \approx \tau_f$, $\tau_r^D = 3.0$ ns and $\tau_r^A = 1.3$ ns (each example has $\langle E \rangle$=0.5). **c**. Corresponding acceptor (*A*) fluorescence lifetime curves (colors as in **a.**). **d**. The full distributions in FRET efficiency *E* are approximated with a discrete distribution with two *E* values. Black line: *E* distribution for Gaussian chain. Red lines: discrete two state *E* distribution with variable amplitudes. The two-state model roughly approximates the bimodal distributions in *E* expected for fluctuating polymers having peaks at high and low *E*. Inset: Same distributions in *R* space. **e**. *E* distribution simulations of *D-A* labeled polymers summarized in plots of standard deviation ΔE versus mean efficiency $\langle E \rangle$. (i) a rigid rod with $\tau_r \approx \tau_f$ and linkers (solid black); with $\tau_r \approx \tau_f$ and no linkers (solid magenta); with $\tau_r \ll \tau_f$ and

linkers (dotted black); and $\tau_r \ll \tau_f$ and no linkers (cyan) (ii) a wormlike chain with L=12 nm and varying l_P: with $\tau_r \approx \tau_f$ and linkers (solid red), with $\tau_r \approx \tau_f$ and no linkers (dotted red); (iii) a Gaussian chain with varying $L \times l_P$: with $\tau_r \approx \tau_f$ and linkers (solid green), with $\tau_r \ll \tau_f$ and linkers (dotted green); and (iv) a hypothetical polymer with the largest possible fluctuations $\Delta E = \sqrt{\langle E \rangle (1 - \langle E \rangle)}$ (solid blue). $\langle E \rangle$ and ΔE corresponding to curves in **b** and **c** shown as colored triangles.

The values of $\langle E \rangle$ and ΔE for different polymer regimes occupy different regions of figure 9e, giving it the "flavor" of a "phase diagram". Predictions from simulations (see *Simulations of Fluorescence Lifetime Decays*) are shown for: (i) rigid rods (magenta and black), (ii) wormlike chains (red), (iii) Gaussian chains (green), and (iv) a hypothetical polymer that switches instantaneously between E=0 and E=1 states (largest possible fluctuations, blue). Colored triangles correspond to fluorescence decays of the same color in figures 9b and 9c.

For rigid rods (i) with rapidly rotating fluorophores ($\tau_r << \tau_f$), $\Delta E = 0$ (cyan triangle). For slower rotational diffusion ($\tau_r \approx \tau_f$), a small ΔE is expected (magenta). Rigid rods with linkers (ii) and $\tau_r \approx \tau_f$ are simulated by varying the distance between *D* and *A* attachment points and keeping r^{tether} constant (solid black).

The wormlike chain regime lies above the rigid rod regime (iii). An example with L=12 nm (varying l_P), $\tau_r \approx \tau_f$, and linkers is shown (solid red). Removing linkers decreases ΔE slightly (dotted red).

The Gaussian chain model (iv) provides an upper limit on the width of distance distributions from soft polymer fluctuations. With $\tau_r \approx \tau_f$ and linkers (varying $L \times l_P$) we obtain the solid green curve. Fluorophore linkers are less important near the Gaussian chain regime, only shifting $\langle E \rangle$ and ΔE along the Gaussian chain curve. Contributions to ΔE from fluctuations in κ^2 and distance do not add linearly. For $\tau_r << \tau_f$, ΔE *increases* (dotted green); the opposite is true for the rigid rod (dotted black);

Model Including Anisotropy and Instrument Response

The model for channels $D_{\text{em,V}}$ and $D_{\text{em,H}}$ are:

$$\begin{aligned} y_{\text{sel}}^{D_{\text{em,V}}}(\tau) &= \text{IRF}_{D_{\text{exc}}}^{D_{\text{em,V}}}(\tau) * f^{D,\text{V}}(\tau) + \Delta_{\text{sel}}^{D_{\text{em,V}}}(\tau) \\ y_{\text{sel}}^{D_{\text{em,H}}}(\tau) &= \text{IRF}_{D_{\text{exc}}}^{D_{\text{em,H}}}(\tau) * f^{D,H}(\tau) + \Delta_{\text{sel}}^{D_{\text{em,H}}}(\tau) \end{aligned} \qquad (4)$$

where $\mathrm{IRF}_{D_{\mathrm{exc}}}^{D_{\mathrm{em,V}}}(\tau)$ and $\mathrm{IRF}_{D_{\mathrm{exc}}}^{D_{\mathrm{em,H}}}(\tau)$ are the measured instrument response functions for detectors $D_{\mathrm{em,V}}$ and $D_{\mathrm{em,H}}$ with the D_{exc} laser. $\Delta_{\mathrm{sel}}^{D_{\mathrm{em,V}}}(\tau)$ and $\Delta_{\mathrm{sel}}^{D_{\mathrm{em,H}}}(\tau)$ are background decay curves obtained using equation (3). $f^{D,\mathrm{V}}(\tau)$ and $f^{D,V}(\tau)$ account for fluorescence decay of D and for fluorescence anisotropy decay $r^{D}(\tau)$,

$$\begin{aligned} f^{D,\mathrm{V}}(\tau) &= \left(1+C_r^{D,\mathrm{V}} r^{D}(\tau)\right) f^{D}(\tau) \\ f^{D,H}(\tau) &= \alpha_{D,V}^{D,H}\left(1+C_r^{D,H} r^{D}(\tau)\right) f^{D}(\tau) \end{aligned} \tag{5}$$

$C_r^{D,\mathrm{V}}$ and $C_r^{D,\mathrm{H}}$ are fluorescence anisotropy amplitude factors that depend on whether the excitation lasers are V or H polarized. Ideally, $C_r^{D,\mathrm{V}}=2$ and $C_r^{D,\mathrm{H}}=-1$ for V excitation, and $C_r^{D,\mathrm{V}}=-1$ and $C_r^{D,\mathrm{H}}=2$ for H excitation. However, polarization mixing caused by the high-NA objective and the dichroic mirror DM2 may change these values. Control fluorescence anistotropy experiments with TMR at micromolar concentrations in varying ratios of water and glycerol indicated that the ideal values were adequate to fit our experiments (not shown). $\alpha_{D,V}^{D,H}$ is the ratio of detection efficiencies for the *H* and *V* channels for *D*, found by comparing ensemble FA measurements using the microscope and a spectrometer. We use a model with two states E_1 and E_2,

$$f^{D}(\tau) = A^{D} N^{D}\left[\beta \exp\left(-\tau/\tau_{f,1}^{D}\right) + (1-\beta)\exp\left(-\tau/\tau_{f,2}^{D}\right)\right] \tag{6}$$

β is the fraction of time spent in state 1. $\tau_{f,1}^{D} = (1-E_1)\tau_{f,0}^{D}$ and $\tau_{f,2}^{D} = (1-E_2)\tau_{f,0}^{D}$. $\tau_{f,0}^{D}$ is the lifetime of D in the absence of *A*. In our experiments, we determine $\tau_{f,0}^{D}$ using the *D*-only subpopulation present in each sample and *D*-only controls. N^{D} is a normalization such that $\int f^{D}(\tau)\,d\tau = A^{D}$. A^{D} is the total number of photons in a channel, correcting for anisotropy and $\alpha_{D,V}^{D,H}$.

$r^{D}(\tau)$ is the donor FA decay, modeled using a single exponential (r_0^{D} is the initial anisotropy and τ_r^{D} is the rotational diffusion timescale):

$$r^{D}(\tau) = r_0^{D}\exp\left(-\tau/\tau_r^{D}\right) \tag{7}$$

We are able to accurately analyze acceptor decays since ns-ALEX allows accurate subtraction of donor leakage into acceptor channels as well as direct excitation of the acceptor for each species in solution. The acceptor decay for $A_{\mathrm{em,V}}$ and $A_{\mathrm{em,H}}$ are:

$$
\begin{aligned}
y_{\text{sel}}^{A_{\text{em,V}}}(\tau) &= \text{IRF}_{A_{\text{exc}}}^{A_{\text{em,V}}}(\tau) * f^{A,V}(\tau) + \Delta_{\text{sel}}^{A_{\text{em,V}}}(\tau) + \\
&\quad \text{IRF}_{D_{\text{exc}}}^{A_{\text{em,V}}}(\tau) * \left[f_E^{A,V}(\tau) + a_A^{A_{em}} f^{A,V}(\tau) + a_D^{A_{em}} f^{D,\text{V}}(\tau) \right] \\
y_{\text{sel}}^{A_{\text{em,H}}}(\tau) &= \text{IRF}_{A_{\text{exc}}}^{A_{\text{em,H}}}(\tau) * f^{A,H}(\tau) + \Delta_{\text{sel}}^{A_{\text{em,H}}}(\tau) + \\
&\quad \text{IRF}_{D_{\text{exc}}}^{A_{\text{em,H}}}(\tau) * \left[f_E^{A,H}(\tau) + a_A^{A_{em}} f^{A,H}(\tau) + a_D^{A_{em}} f^{D,H}(\tau) \right]
\end{aligned}
\tag{8}
$$

$\Delta_{\text{sel}}^{A_{\text{em,V}}}(\tau)$ and $\Delta_{\text{sel}}^{A_{\text{em,H}}}(\tau)$ are found using equation (3). Similar to equation (5),

$$
\begin{aligned}
f^{A,\text{V}}(\tau) &= \left(1 + C_r^{A,\text{V}} r^A(\tau)\right) f^A(\tau) \\
f^{A,H}(\tau) &= \alpha_{A,V}^{A,H} \left(1 + C_r^{A,H} r^A(\tau)\right) f^A(\tau)
\end{aligned}
\tag{9}
$$

We model the intrinsic *A* decay as a single exponential,

$$
f^{A,V}(\tau) = A^A \exp\left(-\tau/\tau_f^A\right)/\tau_f^A \tag{10}
$$

The final τ_f^A normalizes the exponential. The terms in equation (8) convolved with the IRF for D_{exc} sum contributions from FRET ($f_E^{A,V}(\tau)$), direct excitation of *A* by D_{exc} ($a_A^{A_{em}} f^{A,V}(\tau)$), and leakage of *D* emission into A_{em} channels ($a_D^{A_{em}} f^{D,\text{V}}(\tau)$). $a_A^{A_{em}}$ is a scaling factor that compares the intensity of direct excitation of *A* by D_{exc} to the excitation by A_{exc}, determined by *A*-only controls. $a_D^{A_{em}}$ is a scaling factor that accounts for leakage of *D* emission into A_{em} channels, determined by *D*-only controls.

The contribution for FRET, $f_E^{A,V}(\tau)$, is, similar to equation (5), expressed in terms of an intrinsic lifetime decay $f_E^A(\tau)$ multiplied by polarization decays (normally set to 0 since FRET is depolarizing). However, $f_E^A(\tau)$ is modeled differently from equation (6) since the FRET emission must go through a two step process prior to emission: a waiting time on *D*, followed by the lifetime decay of *A*. The same two lifetime components are used from equation (6), but the weighting is different,

$$
f_E^A(\tau) = A^E N^E \left[\beta \exp\left(-\tau/\tau_{f,1}^D\right) E_1/\tau_{f,1}^D + (1-\beta) \exp\left(-\tau/\tau_{f,2}^D\right) E_2/\tau_{f,2}^D \right] * f^A(\tau) \tag{11}
$$

N^E is a normalization such that $\int f^E(\tau) d\tau = A^E$. A^E is the total number of FRET photons in a channel, correcting for anisotropy and $\alpha_{A,V}^{A,H}$.

Figure 10 demonstrates that the two state model adequately fits fluorescence lifetime curves from *D*-*A*-labeled Gaussian chains, and that the $\langle E \rangle$ and ΔE extracted using the fit match the simulation values.

The extracted ΔE values are about 5% too low since we use parameters extracted for a discrete model to describe a continuous distribution. One reason the match is good is that the two-state fitting model is approximating the bimodal *P(E)* distribution polymers have in *E* space (figure 9d), with peaks near *E*=0 and *E*=1. This bimodal distribution arises from the steep distance dependence of FRET. Our simulations are fit using the same model as the experimental data with the same statistical weighting and instrument response so that there is a fair comparison between simulation and experiment.

Figure 11 demonstrates the inadequacy of a fitting model accounting for only one *E* (table 1, fitted parameters) and the adequacy of our two-state model (table 2, fitted parameters). In the tables, the only parameters not discussed above are $\Delta\tau_{D_{\text{exc}}}^{D_{\text{em,V}}}$, $\Delta\tau_{D_{\text{exc}}}^{A_{\text{em,V}}}$, $\Delta\tau_{D_{\text{exc}}}^{D_{\text{em,H}}}$, $\Delta\tau_{D_{\text{exc}}}^{A_{\text{em,H}}}$, $\Delta\tau_{A_{\text{exc}}}^{A_{\text{em,V}}}$, and $\Delta\tau_{A_{\text{exc}}}^{A_{\text{em,H}}}$, fitted shifts in the IRF for the detectors (necessary due to drifts in detectors and timing electronics over time).

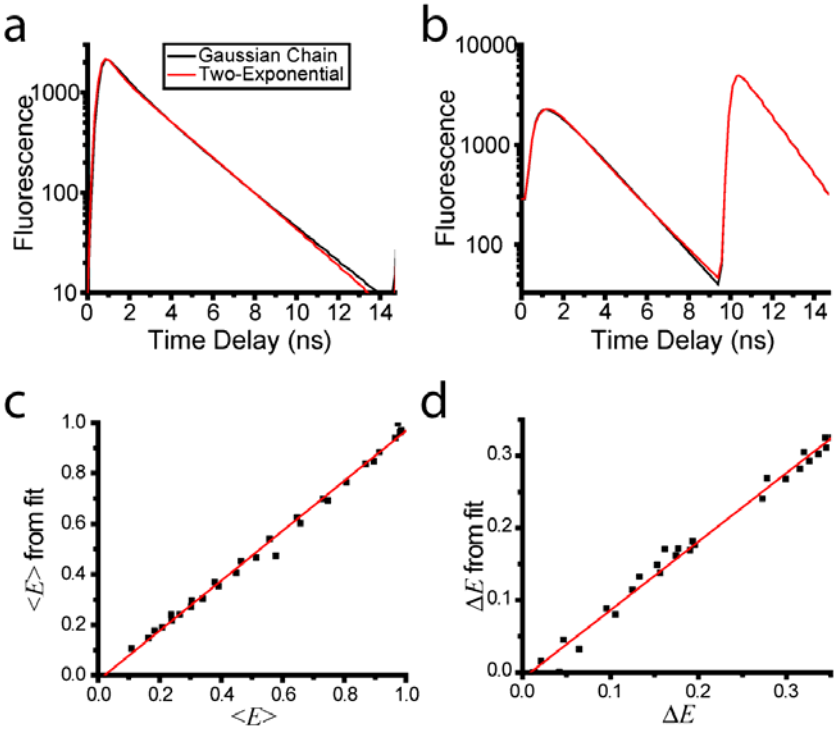

Fig. 10. a. Black: Donor lifetime decay for a *D-A*-labeled Gaussian chain. Red: Fit of black decay using two state model. **b.** Acceptor lifetime decay and fit. The first decay is for D_{exc} and the second decay is for A_{exc}. **c.** Black: comparison of $\langle E \rangle$ determined from fit versus $\langle E \rangle$ determined directly from simulations. Red: Fit to linear model, $\langle E \rangle_{\text{fit}} = 0.99\langle E \rangle_{\text{sim}} - 0.02$. **d.** Black: comparison of ΔE determined from fit versus ΔE determined directly from simulations. Red: Fit to linear model, $\Delta E_{\text{fit}} = 0.95\Delta E_{\text{sim}} - 0.01$.

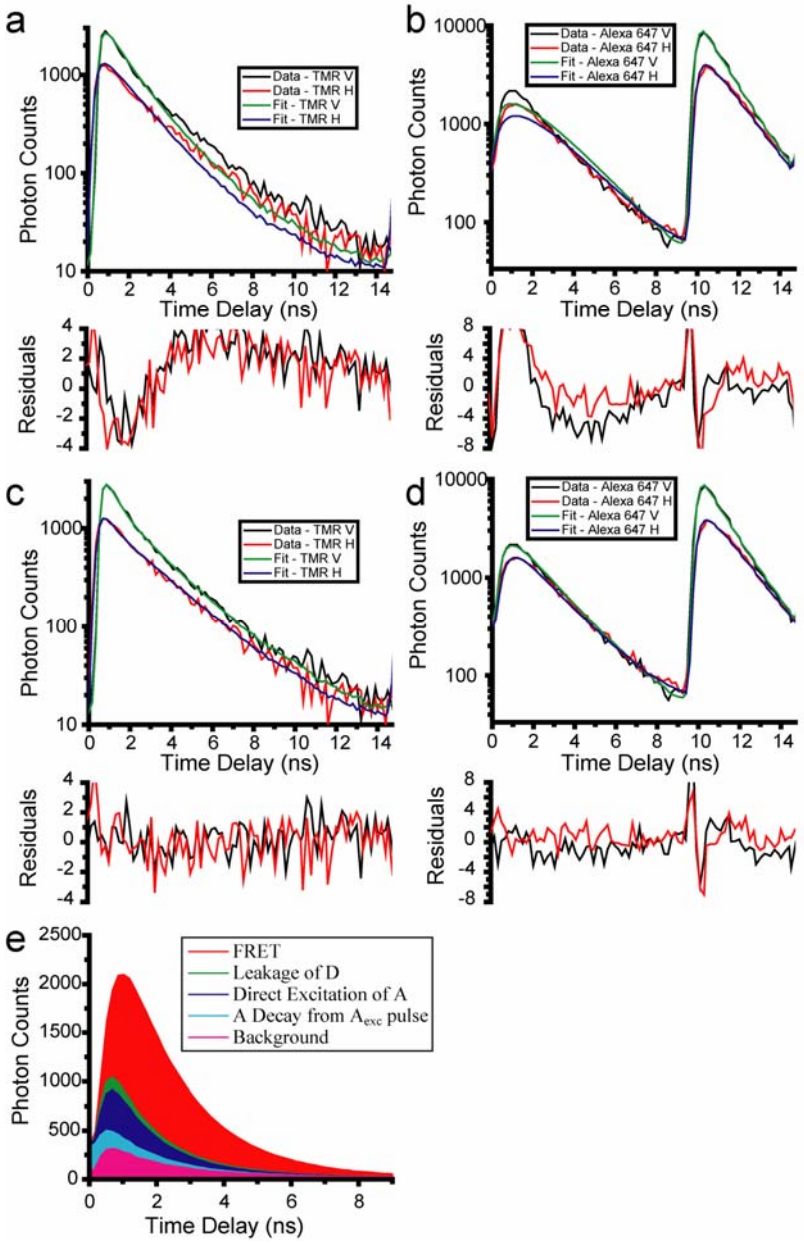

Fig. 11. Lifetime decay curves and fits for $(dT)_{30}$ for [NaCl]=1M. **a.** Donor lifetime curves and one *E* state model. Black: donor data for polarization parallel to excitation. Green: Fit with one *E* state. Red: donor data for perpendicular polarization. Blue: Fit with one *E* state. Residuals are plotted below graph. **b.** Acceptor lifetime curves. **c.** Same as A, except green and blue curves corresponds to two-state model fit. **d**. Same as B, except now with two-state model fit. **e.** Shows the various contributions to the decay caused by D_{exc} in the acceptor channel accounted for in fit. Red: FRET. Green: leakage of *D* photons into *A* channel. Blue: direct excitation of *A* by D_{exc} laser. Cyan: Leakage of *A* decay from A_{exc} laser into region of D_{exc} laser (can be decreased by lengthening nsALEX alternation period beyond 14.7 ns). Magenta: background photons accounted for by equation (3).

Table 1: Fit parameters for mono-exponential fit in figure 11a-b

Parameter Name	Parameter Value	Nominal error
$\Delta\tau_{D_{exc}}^{D_{em,V}}$ - IRF time shift	6.201443	0.154
$\Delta\tau_{D_{exc}}^{A_{em,V}}$ - IRF time shift	-1.215729	0.260
$\Delta\tau_{D_{exc}}^{D_{em,H}}$ - IRF time shift	-661.080841	0.231
$\Delta\tau_{D_{exc}}^{A_{em,H}}$ - IRF time shift	-4.073238	0.348
$\Delta\tau_{A_{exc}}^{A_{em,V}}$ - IRF time shift	-101.004718	0.085
$\Delta\tau_{A_{exc}}^{A_{em,H}}$ - IRF time shift	-101.634691	0.137
A^D	57187.128692	213.199
$\tau_{f,0}^D$	3.200000	Fixed
$\tau_{f,1}^D$	1.524254	0.006
$\tau_{f,2}^D$	Undefined	Fixed
β	0	Fixed
$a_D^{A_{em}}$	0.060944	Fixed
$\alpha_{D,V}^{D,H}$	0.840000	Fixed
τ_r^D	1.643214	0.118
$2r_0^D$	0.433799	0.013
A^A	191717.168709	381.412
τ_f^A	1.409877	0.004
A^D	0.060000	Fixed
$\alpha_{A,V}^{A,H}$	0.840000	Fixed
τ_r^A	2.241476	0.100
$2r_0^A$	0.393343	0.006
A^E	63371.418733	252.092
$\tau_{r,\mathrm{FRET}}^A$	1.008703	Fixed
$2r_{0,\mathrm{FRET}}^A$	0.000000	Fixed

Table 2: Fit parameters for bi-exponential fit in figure 11c-e

Parameter Name	Parameter Value	Nominal error
$\Delta\tau_{D_{exc}}^{D_{em,V}}$ - IRF time shift	7.236814	0.144
$\Delta\tau_{D_{exc}}^{A_{em,V}}$ - IRF time shift	6.725332	0.262
$\Delta\tau_{D_{exc}}^{D_{em,H}}$ - IRF time shift	-660.971635	0.240
$\Delta\tau_{D_{exc}}^{A_{em,H}}$ - IRF time shift	8.518467	0.340
$\Delta\tau_{A_{exc}}^{A_{em,V}}$ - IRF time shift	-101.230515	0.088
$\Delta\tau_{A_{exc}}^{A_{em,H}}$ - IRF time shift	-103.023825	0.140
A^D	58941.804563	217.858
$\tau_{f,0}^D$	3.200000	Fixed
$\tau_{f,1}^D$	2.133218	0.014
$\tau_{f,2}^D$	0.388777	0.011
β	0.523194	0.006
$a_D^{A_{em}}$	0.060944	Fixed
$\alpha_{D,V}^{D,H}$	0.840000	Fixed
τ_r^D	1.826296	0.116
$2r_0^D$	0.469268	0.012
A^A	192412.480129	381.584
τ_f^A	1.490129	0.004
A^D	0.060000	Fixed
$\alpha_{A,V}^{A,H}$	0.840000	Fixed
τ_r^A	1.705556	0.066
$2\,r_0^A$	0.440220	0.007
A^E	67126.070778	256.806
$\tau_{r,\mathrm{FRET}}^A$	Undefined	Fixed
$2\,r_{0,\mathrm{FRET}}^A$	0.000000	Fixed

Simulations of Fluorescence Lifetime Decays

In the FRET measurements described in this study, *D* is excited by a linearly polarized laser, and *A* is excited by energy transfer from *D*. We simulate expected lifetime decays for these measurements by solving the coupled first order differential equations

$$\begin{aligned}\frac{dP_D(t)}{dt} &= \left[-\frac{1}{\tau_f^D} - k_{\text{FRET}}(t)\right] P_D(t) \\ \frac{dP_A(t)}{dt} &= -\frac{1}{\tau_f^A} P_A(t) + k_{\text{FRET}}(t) P_D(t),\end{aligned} \tag{12}$$

with initial conditions $P_D(0) = 1$ and $P_A(0) = 0$. $P_D(t)$ and $P_A(t)$ are, respectively, the singlet-excited state populations of *D* and *A*. τ_f^D and τ_f^A are, respectively, the intrinsic fluorescence lifetimes of the singlet excited states of *D* and *A*. $k_{\text{FRET}}(t)$ is the rate of energy transfer from *D* to *A*,

$$k_{\text{FRET}}(t) = \frac{1}{\tau_f^D}\left(\frac{R_0}{R(t)}\right)^6 \frac{\kappa^2(t)}{2/3} \tag{13}$$

$R(t)$ is the distance between *D* and *A* as a function of time *t*. R_0 is the distance at which energy transfer efficiency E is 50%, assuming $\kappa^2 = 2/3$. To account for fluorophore orientational dynamics, we multiply by $\frac{\kappa^2(t)}{2/3}$.

An inappropriate expression, $k_{\text{FRET}}(t) = \frac{1/\tau_f^D}{1 + (R/R_0)^6}$, has recently been used in modeling FRET in the presence of polymer dynamics(3, 4). The modification was made to avoid the divergence at $R = 0$ in equation (13). However, this modification leads to incorrect results: the maximum FRET rate is only $1/\tau_f^D$, leading to a maximum *E* of 0.5. In fact, $k_{\text{FRET}}(t)$ can be much larger than $1/\tau_f^D$. If the divergence at $R = 0$ is problematic, an expression such as $k_{\text{FRET}}(t) = \frac{k_F}{\varepsilon + (R/R_0)^6}$ should be used, where $\varepsilon \ll 1$.

The observable quantities in fluorescence lifetime measurements, the rates of photon detection, are calculated from the excited state populations, $k_D(t) = \frac{Q_D}{\tau_f^D} P_D(t)$ and $k_A(t) = \frac{Q_A}{\tau_f^A} P_A(t)$. Q_D and Q_A are

quantum efficiencies of the respective fluorophores. These rates are split into polarization components parallel and perpendicular to the excitation laser:

$$
\begin{aligned}
k_{D,\|}(t) &= \frac{Q_D}{\tau_f^D} P_D(t) \cos\theta_D(t) \\
k_{D,\perp}(t) &= \frac{Q_D}{\tau_f^D} P_D(t) \sin\theta_D(t) \cos\phi_D(t) \\
k_{A,\|}(t) &= \frac{Q_A}{\tau_f^A} P_A(t) \cos\theta_A(t) \\
k_{A,\perp}(t) &= \frac{Q_A}{\tau_f^A} P_A(t) \sin\theta_A(t) \cos\phi_A(t)
\end{aligned}
\qquad (14)
$$

(θ_D, ϕ_D) and (θ_A, ϕ_A) are angular variables for the dipole orientations of *D* and *A*, respectively. For $\theta_D = 0$ or $\theta_A = 0$, the respective dipole is aligned with the excitation polarization.

Solving equation (12) and calculating $k_{D,\|}(t)$, $k_{D,\perp}(t)$, $k_{A,\|}(t)$, and $k_{A,\perp}(t)$ provides the expected lifetime curve for only one "path" of the functions $R(t)$ and $\kappa^2(t)$. To obtain the observable lifetime decay curves, we average the solutions for many paths $R(t)$ and $\kappa^2(t)$ calculated using Monte Carlo simulation (10000 paths used, simulation time step Δt is 17 ps). These averaged solutions are then convolved with the experimental instrument response functions, and fitted using the model in *Model Including Anisotropy and Instrument Response*.

Simulating $\kappa^2(t)$ Using Rotational Diffusion of Fluorophore Dipole Orientations. Dipole orientation restrictions and rotational diffusion on time scales near the fluorescence lifetime shift and widen $P(E)$ (5, 6). We assume that the fluorophores have complete rotational freedom, and that fluorescence anisotropy results from rotational diffusion of the fluorophores on time scales similar to the fluorescence lifetime. We emphasize that we *do not* assume a dynamic averaged value of $\langle \kappa^2 \rangle = 2/3$. We assume that on long time scales (after conformational relaxation of the entire polymer chain), there is no preferred relative orientations of the fluorophores. This means that ΔE is increased due to effects of κ^2. For ssDNA and unfolded protein, the chains are unstructured, so this is a good assumption(6). This argument does not necessarily hold in the case of dsDNA, but we obtain a reasonable match in dependence of $\langle E \rangle$ on distance (figure 3).

We further simplify the analysis by assuming that the rotational diffusion can be explained by an isotropic, spherical rotor. Our time-resolved anisotropy decay curves indicate significant rotation on the same time scale as fluorescence lifetime (table 3). We use simulations of the rotational diffusion of a spherical rotor using the extracted diffusion rates. Simulating the rotational diffusion of *D* and *A* using spherical rotors leads to the maximum initial anisotropy amplitude of 0.4, which is higher than the initial measured anisotropies (amplitudes listed are $2r_0$). Hence, we likely overestimate the effects of the rotational diffusion on ΔE (the differences are still not large).

Table 3: Rotation timescale/ amplitude

	Donor rotation time scale	Donor rotation amplitude	Acceptor rotation time scale	Acceptor rotation amplitude
ssDNA $(dT)_{30,}$300mM NaCl	1.8 ± 0.3	0.5 ± 0.2	2.4 ± 1.0	0.41 ± 0.06
ssDNA $(dT)_{40,}$300mM NaCl	3.2 ± 0.2	0.43 ± 0.01	1.9 ± 0.1	0.42 ± 0.02
ssDNA $(dT)_{50,}$300mM NaCl	2.7 ± 0.0	0.46 ± 0.00	1.4 ± 0.1	0.43 ± 0.05
dsDNA, T1B18	3.0 ± 0.6	0.63 ± 0.04	1.3 ± 0.0	0.65 ± 0.01
CI2, 5M GdnCl	2.9 ± 0.2	0.62 ± 0.01	4.9 ± 1.0	0.50 ± 0.01
ACBP, 5M GdnCl	8.9 ± 3.5	0.27 ± 0.08	1.8 ± 0.1	0.47 ± 0.01

The data points are averages of two or three independent experiments, error bars are standard error of the mean

The initial dipole orientation of *D* is drawn from the distribution $P_D\left(\theta_D,\phi\right)_D d\phi_D d\cos\theta_D = \frac{3}{2}\cos^2\theta_D d\phi_D d\cos\theta_D$. The initial dipole orientation of *A* is equally likely to point in any direction, $P_A\left(\theta_A,\phi_A\right)d\phi_A d\cos\theta_A = d\phi_A d\cos\theta_A$.

We use a fixed angular step size a at each time step Δt to simulate rotational diffusion. The dipole has an initial orientation $\left(\theta,\phi\right)$ with respect to the z axis. We set $\phi = 0$ without loss of generality. At each time step Δt, the dipole orientation changes by an angle a, with a random direction, specified by the angle α (α is random with a uniform distribution between 0 and 2π). These angles are illustrated in figure 12.

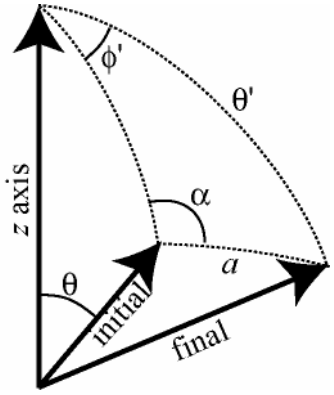

Fig. 12. Angle definitions for rotational diffusion simulations.

Given $\theta, \alpha,$ and a, we determine the new (θ', ϕ') using the law of cosines and sines for spherical angles, obtaining

$$\begin{aligned} \cos\theta' &= \cos\theta\cos a + \sin\theta\sin a\cos\alpha \\ \cos\phi' &= \frac{\cos a - \cos\theta\cos\theta'}{\sin\theta\sin\theta'} \\ \sin\phi' &= \sin\alpha\frac{\sin a}{\sin\theta'} \end{aligned} \tag{15}$$

There are a few special cases, where these formulas have singularities:

$$\begin{aligned} &\text{if } \theta = 0, \text{ set } \theta' = a, \phi' = \alpha \\ &\text{if } \theta = \pi, \text{ set } \theta' = \pi - a, \phi' = -\alpha \\ &\text{if } \theta' = 0 \text{ or } \pi, \text{ set } \phi' = 0 \end{aligned} \tag{16}$$

We calibrate the rotational diffusion simulations using simulated fluorescence anisotropy measurements, comparing the intensity of light detected parallel and perpendicular to the excitation polarization, $r = \frac{I_{\parallel} - I_{\perp}}{I_{\parallel} + 2I_{\perp}}$. Initial dipole orientations are randomly drawn from the distribution, $P(\theta,\phi)\,d\phi\,d\cos\theta = \frac{3}{2}\cos^2\theta\,d\theta\,d\phi\,d\cos\theta$.

The dipole orientations are changed at each time step using the fixed angular step size *a*, as described above, while the fluorescence is decaying with lifetime τ. The fluorescence intensities $I_{\parallel}$ and $I_{\perp}$ are calculated after averaging over 10000 rotational diffusion paths. The anisotropy *r* is calculated, and converted into the rotational diffusion constant D_{rot} using the Perrin equation, $\frac{r_0}{r} = 1 + 6D_{\text{rot}}\tau$, where D_{rot} is the rotational diffusion constant, the fundamental anisotropy is r_0, and the fluorescence lifetime

is $\tau = 1$ ns. The excitation and emission dipoles are collinear in the simulations, so $r_0 = 0.4$. Based on the isotropic rotational diffusion equation, $\frac{\partial P(\theta,\phi)}{\partial t} = -D_{\text{rot}}\left(\frac{\partial^2}{\partial\theta^2} + \frac{1}{\tan\theta}\frac{\partial}{\partial\theta} + \frac{1}{\sin^2\theta}\frac{\partial^2}{\partial\phi^2}\right)P(\theta,\phi)$, the functional relationship between the infinitesimal fixed step size a and D_{rot} should be quadratic, $D_{\text{rot}}\tau = ka^2/\Delta t$. In our calibration fit in figure 13, we add an additional term to account for nonlinear effects with non-infinitesimal angular step sizes for *a*.

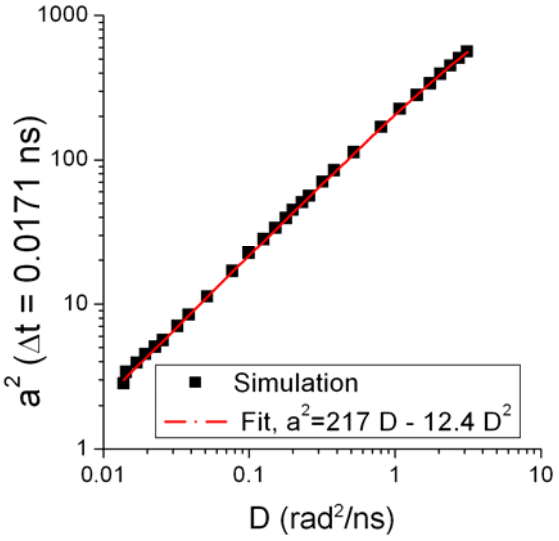

Fig. 13. Calibration of rotational diffusion simulations. The square of the angular step size *a* is plotted versus the diffusion constant *D*, and fit to a quadratic function.

FRET depends on the relative dipole orientations of *D* and *A* through the factor

$$\kappa^2 = \left(\cos\theta_T' - 3\cos\theta_D'\cos\theta_A'\right)^2 \qquad (17)$$

where θ_D' and θ_A' are the angles between the separation vector $\vec{R}$, and *D* and *A*, respectively, and θ_T' is the angle between *D* and *A*. Rapid rotational diffusion of *D* and *A* gives an averaged value of $\langle\kappa^2\rangle = 2/3$. When this assumption cannot be made, we calculate a series of paths $\kappa^2(t)$, with time resolution Δt. The trigonometric functions in equation (17) are now expressed in the coordinates where $\theta_D = \theta_A = 0$ corresponds to the excitation polarization,

$$\begin{aligned}
\cos\theta_T' &= \cos\theta_D\cos\theta_A + \sin\theta_D\sin\theta_A\cos(\phi_D - \phi_A)\\
\cos\theta_D' &= \cos\theta_D\cos\theta_R + \sin\theta_D\sin\theta_R\cos(\phi_D - \phi_R)\\
\cos\theta_A' &= \cos\theta_A\cos\theta_R + \sin\theta_A\sin\theta_R\cos(\phi_A - \phi_R)
\end{aligned} \qquad (18)$$

(θ_R, ϕ_R) are the angular variables for the direction of the D-A separation vector $\vec{R}$ in the same coordinate system. The initial orientation of $\vec{R}$ is equally likely to point in any direction, $P_R(\theta_R, \phi_R)\, d\phi_R d\cos\theta_R = d\phi_R d\cos\theta_R$

The rotational diffusion times τ_r^D and τ_r^A for *D* and *A* are obtained from the fits described in *Model Including Anisotropy and Instrument Response*. They are converted into D_{rot}^D and D_{rot}^A using the equation, $\tau_r = 1/6D_{\text{rot}}$. Using the calibration from figure 13, we obtain the step size *a* to use in the rotational diffusion simulations. These relations assume only a single rotational diffusion time. We miss any faster fluorescence anisotropy decay times, overestimating orientational effects.

Simulating $R(t)$ Using Static Polymer Models and Calibration of Linker Contribution. For most of the simulations, we assume that the distance fluctuations of the polymer occur on time scales slower than the fluorescence lifetime. With this assumption, each simulated distance path is replaced by a single value, $R(t) = R$. For each path, a random value for *R* is drawn from a probability distribution from one of the polymer models discussed in the main text.

The long, flexible linkers attaching the fluorophores to the macromolecules under study are modeled using a Gaussian chain, in addition to the polymer end-to-end distance above. We use the root-mean-square (rms) distance, $r_{\text{rms}}^{\text{linker}} = \sqrt{l_P^{\text{linker}} L^{\text{linker}}}$, to describe the length of the linkers. In the simulation, three Gaussian random numbers x,y, and z are generated (one for each axis) for Gaussian chain model from $P(R) = 4\pi R^2 \exp\left(-3R^2/4l_P^{\text{linker}} L^{\text{linker}}\right)\left(3/4\pi l_P^{\text{linker}} L^{\text{linker}}\right)^{\frac{3}{2}}$ with rms distance $r_{\text{rms}}^{\text{linker}}$. The modified distance with the linker is calculated, $R^{+\text{linker}} = \sqrt{(R+x)^2 + y^2 + z^2}$.

We use a grid of rigid rod simulations that include linkers and rotational diffusion of *D* and *A* in comparison with our dsDNA data to calibrate the effective size of the linkers (figure 14). For the simulations, there is a fixed distance *R* between the *D* and *A* "attachment points." In figure 14, the values for $r_{\text{rms}}^{\text{linker}}$ that best match the data for high $\langle E \rangle$ is $r_{\text{rms}}^{\text{linker}} = 1.3 \pm 0.1$ nm. The error estimate is obtained by comparing variations from repeated measurements and for different *D*-*A* separations.

One possible explanation for the increased ΔE (with $r_{\text{rms}} = 2.1 \pm 0.1$ nm) for *D*-*A* separations of 22 and 27 base pairs is fraying of the ends of dsDNA. Crudely subtracting the contribution from the fluorophore and tether (1.3 nm), a minimum of 2 bases (0.7 nm = 2 bases * 0.34 nm) of fraying is

required to explain the high ΔE (assuming the frayed bases remain rigid). Other possible explanations are mentioned in the main text. Exploring the cause of the high ΔE will be the topic for a future study.

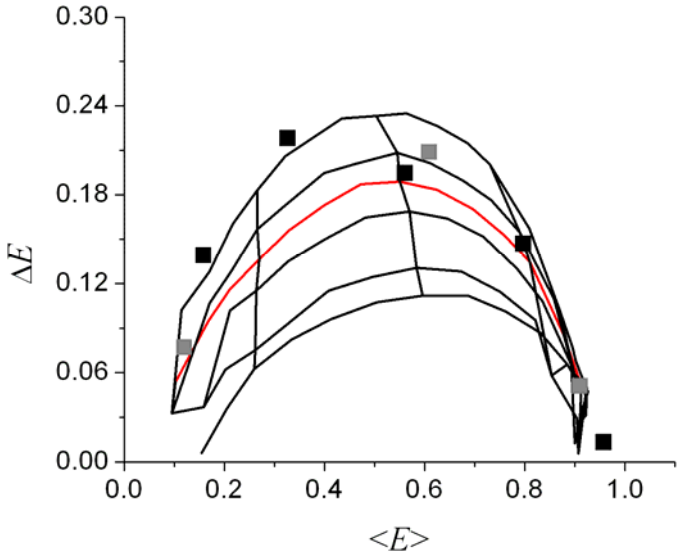

Fig. 14. ΔE vs. $\langle E \rangle$ derived from experiments on *D-A* labeled dsDNA with 7,12,17,22, and 27 base pair *D-A* separations (black squares) and internally labeled dsDNA with 5,15, and 25 base pair *D-A* separations (gray squares). Black: grid of rigid rod simulations accounting for slow rotational diffusion with values for $r_{\mathrm{rms}}^{\mathrm{linker}} = \sqrt{l_P^{\mathrm{linker}} \times L^{\mathrm{linker}}}$, starting from the bottom, 0, 0.5, 1.0, 1.25, 1.5, and 2 nm. The vertical lines indicate constant distance between fluorophore attachment points. The simulations with $r_{\mathrm{rms}}^{\mathrm{linker}} = 1.25$ nm are shown in red (chosen to be closest to black squares). For the dsDNA with 7,12, and 17 base pair *D-A* separations, we obtain $r_{\mathrm{rms}}^{\mathrm{linker}} = 1.3 \pm 0.1$ nm. For the 22 and 27 base pair *D-A* separations, we obtain $r_{\mathrm{rms}} = 2.1 \pm 0.1$ nm, likely containing contributions beyond the fluorophore linker. The gray squares are closer to the $r_{\mathrm{rms}}^{\mathrm{linker}}$=1.5 nm line. However, R_0 for the internally labeled dsDNA is smaller than for the dsDNA with end-labeled *D* (about 90%). Accounting for this, $r_{\mathrm{rms}}^{\mathrm{linker}} = 1.4 \pm 0.1$ nm, consistent with the value for the other dsDNA series. In the main text and in the simulations we use the first value, $r_{\mathrm{rms}}^{\mathrm{linker}} = 1.3 \pm 0.1$ nm.

Simulating $R(t)$ Using Dynamic Polymer Models. We use two methods to obtain fluctuating $R(t)$ to understand the extent of conformational dynamics within the fluorescence lifetime of *D*.

The first method uses 1D Brownian Dynamics simulations(7) within a potential well defined by the end-to-end distance distribution $P(R)$. $N(R,t)$, the time-varying probability distribution of the end-to-end distance, satisfies the following Fokker-Planck equation(8),

$$\frac{\partial N(R,t)}{\partial t} = \frac{\partial}{\partial r} D \left(\frac{\partial N(R,t)}{\partial r} - N(R,t) \frac{\partial}{\partial r} \ln P(R) \right) \qquad (19)$$

D is the end-to-end diffusion constant of the polymer chain. A starting guess for the value of D is double the free diffusion constant for one subunit (one base or one amino acid). For Brownian dynamics simulations, random trajectories with time resolution Δt are formed using equation (19). At each time step i the position $R = R_i$ is known; hence, the probability distribution is $N(R, i\Delta t) = \delta(R - R_i)$. The probability distribution for the change in R (ΔR) at the next step is determined by solving equation (19) to first order, giving a Gaussian distribution with mean $\langle \Delta R \rangle = \frac{\partial}{\partial r} \ln P(R) \Big|^{R=R_i}$ and variance $\langle \Delta R^2 \rangle - \langle \Delta R \rangle^2 = 2D\Delta t$ (7). Using a Gaussian random number generator, the next position R_{i+1} is chosen. Repeating this process, a full trajectory $R(t)$ is simulated.

We present here a series of simulations that help interpret the ssDNA data (figure 15), where the issue of conformational dynamics is particularly important. The series of simulations covers 4 possible base-to-base distances (h=0.4, 0.5, 0.6, and 0.7 nm/base), 3 contour lengths (30, 40, and 50 bases), 15 values of persistence length (L/l_P between 0.5 and 40), and 3 values for D. Using a hydrodynamic radius of $a = 0.3\text{nm}$ for dT, and $\zeta = 6\pi\eta a$ with $\eta = 1$ cp, we get $D_{\text{free}} = kT/\zeta = 7.3\times10^{-6}\ \text{cm}^2/\text{s}$; this is in agreement with experimental determinations(9). Doubling this, we use $D = 1.5\times10^{-5}\ \text{cm}^2/\text{s}$ for one value of D. For a second value we use ten times lower, $D = 1.5\times10^{-6}\ \text{cm}^2/\text{s}$; for a third value, $D = 0\,\text{cm}^2/\text{s}$.

These simulations were performed without accounting for linkers; the overall statistics were not affected much by this (compare solid and dotted red, purple, and cyan lines in upper left panel). The main effect of conformational dynamics within the fluorescence lifetime is to shift ΔE down and $\langle E \rangle$ to the right (compare movement of dotted lines of right panels versus the middle and left panels). The reduction of ΔE compared to the Gaussian chain limit (green line) is clearly stronger for higher $\langle E \rangle$ than for lower $\langle E \rangle$; this is the opposite of what is observed for the ssDNA experiments. The only satisfactory matches to the ssDNA data are in the top panels on the left and the middle. By interpolating between the simulations shown and comparing to the ssDNA data, we obtain the ranges $0.4\ \text{nm} < h < 0.45\ \text{nm}$ and $0\ \text{cm}^2/\text{s} < D \le 1.5\times10^{-6}\ \text{cm}^2/\text{s}$ used in the main text. For example, the $(\text{dT})_{30}$ data is best matched using h=0.4 nm with $D = 0\,\text{cm}^2/\text{s}$. However, a match nearly as good can be obtained by interpolating halfway between the results for h=0.4 nm and h=0.5 nm and $D = 1.5\times10^{-6}\ \text{cm}^2/\text{s}$. The $(\text{dT})_{40}$ and $(\text{dT})_{50}$ data indicate a similar range in possible values.

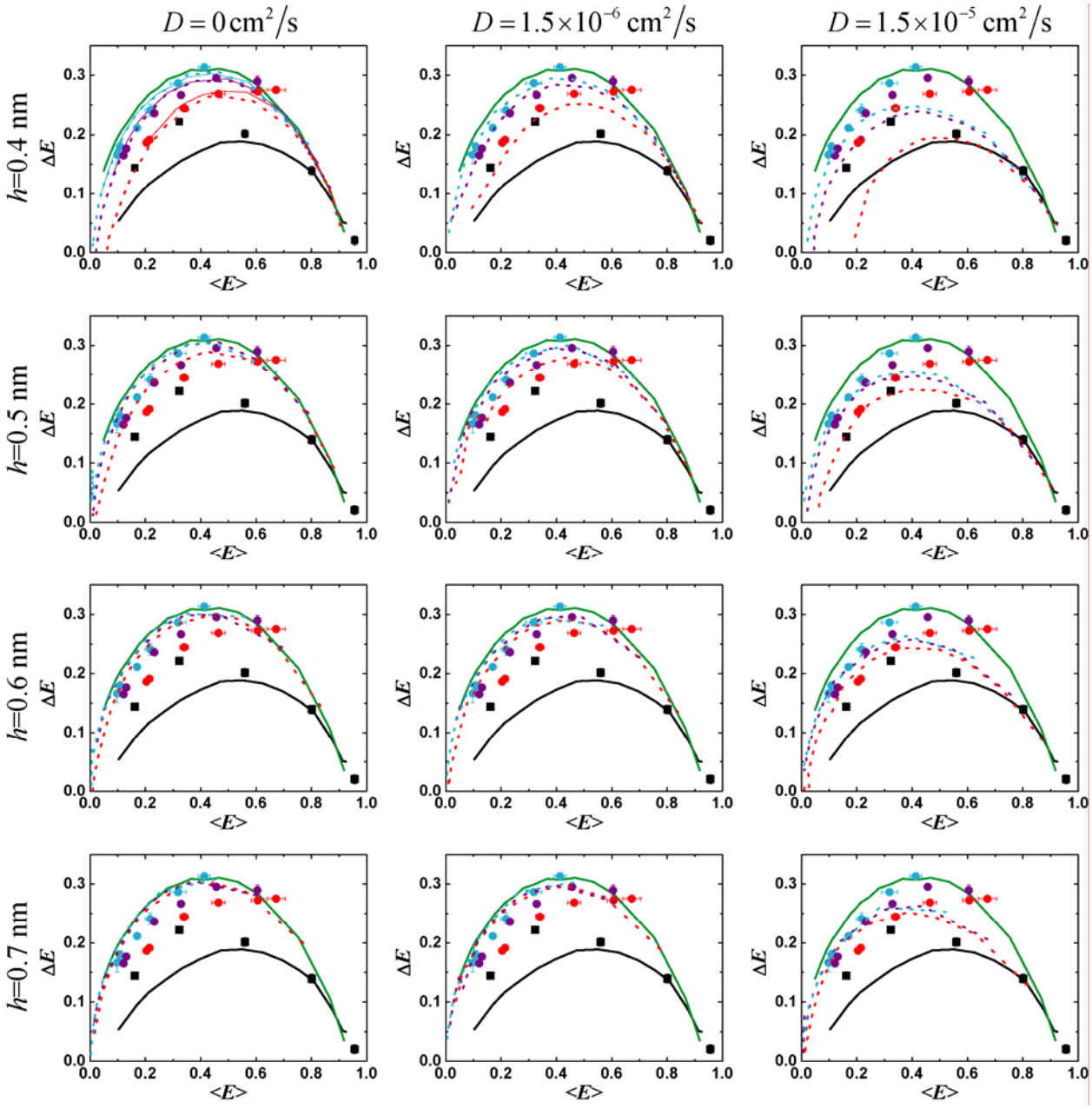

Fig. 15. Polymer dynamics on the same time scale as the donor fluorescence lifetime can affect FRET measurements. From figure 1 (main text): ΔE vs. $\langle E \rangle$ extracted from experiments on *D-A* labeled biopolymers: dsDNA with 7,12,17,22, and 27 base pair *D-A* separations (black squares); ssDNA at varying salt concentration ($(dT)_{30}$, red circles; $(dT)_{40}$, opurple circles; $(dT)_{50}$, cyan circles). Simulations with linkers (from figure 1): (i) a rigid rod with $\tau_r \approx \tau_f$ and linkers (solid black); (ii) a wormlike chain with *L*=12 nm, varying l_P, $\tau_r \approx \tau_f$ and linkers (solid red, upper left panel); (iii) a wormlike chain with *L*=16 nm (solid purple, upper left panel); (iv) a wormlike chain with *L*=20 nm (solid cyan, upper left panel); and (v) a Gaussian chain with varying Ll_P, $\tau_r \approx \tau_f$ and linkers (solid green). ΔE vs. $\langle E \rangle$ for simulations of wormlike chains with $\tau_r \approx \tau_f$ and no linkers undergoing conformational dynamics within the fluorescence lifetime for: 30 bases (dotted red), 40 bases (dotted purple), and 50 bases (dotted cyan), each with varying l_P. The contour length for each line is found

by $L = h \times$ number of bases , where h is the average base-to-base distance written on the left of the figure, and D is the diffusion constant listed at the top of the figure.

The above method may use any end-to-end distance distribution, but assumes the dynamics can be represented as diffusion in a 1D potential. The second method we use to simulate $R(t)$ is a Rouse-Zimm model, which assumes a Gaussian chain distribution, but simulates the polymer dynamics in 3D. Our method is similar to (3). We use the normal mode amplitudes and time scales from both the Rouse model and the Zimm model (which accounts for hydrodynamic effects, as described in (10)). We performed a series of dynamic simulations on polymer chains, and in figure 16 plot them over the simulations from figure 1. The simulations were performed for a static Gaussian chain, L=20 nm, and, in order of increasing $\langle E \rangle$ in figure 16, l_P =3.2 nm, 1.25 nm, and 0.6 nm. By adding Rouse dynamics with T=300 K, $\eta = 0.001$ kg m/s (water), and sphere diameter b=2l_P , we obtain the black circles. Using Zimm dynamics with the same parameters, we obtain the inverted blue triangles. Significant increases in $\langle E \rangle$ and decreases in ΔE are observed, with similar magnitudes to those found in figure 15.

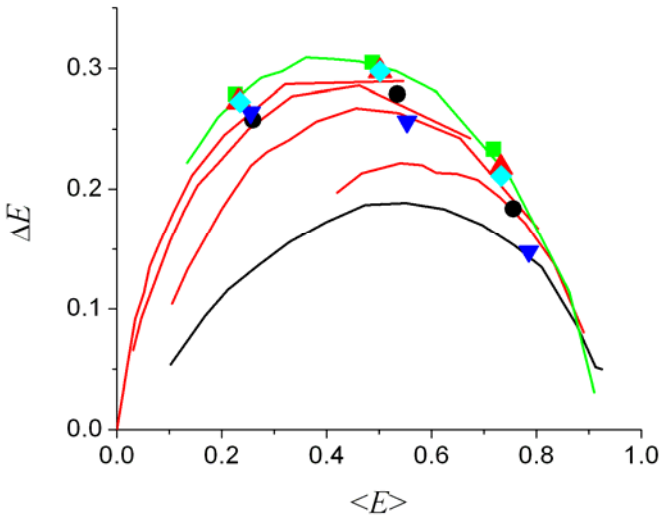

Fig. 16. Effects of polymer dynamics on ΔE vs. $\langle E \rangle$ plotted on simulations from figure 1b (green, red, and black lines). Green squares: static Gaussian chain models. Black circles: Rouse model with diffusion rates for free water. Blue inverted triangles: Zimm model with diffusion rates for free water. Red triangles: Rouse model with diffusion accounting for intrachain viscosity. Cyan diamonds: Zimm model with diffusion accounting for intrachain viscosity.

However, from our simulations above, and from measurements of fluorescence or phosphorescence contact quenching, the intrachain diffusion rates are estimated to be at least an order of magnitude slower than free diffusion rates for both polypeptides (11) and nucleic acids (performed only for small number of bases - 2 or 4) (12). Repeating the simulations with $\eta = 0.01$ kg m/s , to slow down the

intrachain diffusion rates, we obtain the red triangles for the Rouse model and the cyan diamonds for the Zimm model. With this slower diffusion, the effects on $\langle E \rangle$ and ΔE are small, near the measurement error. Based on both sets of simulations, we expect dynamics of the polymer chains within the fluorescence lifetime to play a minor role in our data.

Assessment of Photophysical Artifacts

The choice of fluorophores for *D* and *A* are critical for obtaining the maximum information possible from nsALEX. Factors that influenced our decisions on fluorophores include brightness, photostability, mono-exponential lifetimes, large spectral separation of *D* and *A* and the Förster radius R_0. The brightness and photostability are evaluated by analyzing acquired data using burst analysis and fluorescence correlation spectroscopy (FCS). The TMR-Alexa 647 pair has all the benefits of the TMR-Cy5 dye pair commonly used in single-molecule FRET measurements, including large signals and a large R_0 (6.9 nm). In addition, Alexa 647 is more photostable than Cy5. The Alexa 532-Alexa 647 dye pair was chosen to improve the spectral separation of the fluorophores (reducing leakage of the *D* signal into *A* detectors) while retaining a relatively large R_0.

Are the Intrinsic Donor and Acceptor Lifetimes Mono-Exponential? We assume in our models that the intrinsic donor and acceptor lifetimes are single-exponential. A single-exponential fit was also adequate for every *A* decay from the A_{exc} laser we measured (for example, see figure 11). In control samples labeled with only *D* (figure 17) and in *D*-only subpopulations, we did not observe any evidence of multi-exponential lifetimes.

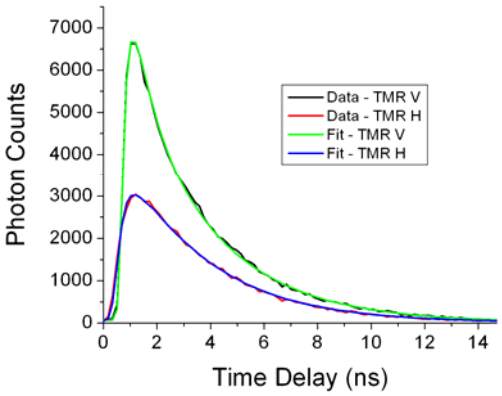

Fig. 17. Single-exponential fit for *D*-only control sample for dsDNA (Polarization effects also taken into account). No evidence of multiple exponents is found.

Tables 4-6 list donor lifetime and acceptor lifetime values found for the ssDNA, CI2, and ACBP. For all tables, the data points are averages of two or three independent experiments, error bars are standard error

of the mean. For dsDNA, all five molecules have their donors labeled at the same position (1) so there is only one donor only sample which gave us 4.0 ± 0.1 ns lifetime. For the series of three internally labeled dsDNA molecules, the donor only samples gave a lifetime of 3.1 ± 0.1 ns.

Table 4: ssDNA: control sample was T30 labeled only with TMR

[NaCl]	1mM	10mM	100mM	300mM	1M	2M
Donor Lifetime	3.6 ± 0.1	3.6 ± 0.1	3.6 ± 0.0	3.6 ± 0.1	3.6 ± 0.2	3.7 ± 0.1
Acceptor Lifetime	1.4 ± 0.2	1.4 ± 0.2	1.2 ± 0.0	1.2 ± 0.0	1.4 ± 0.0	1.5 ± 0.0

Table 5: CI2 1-53: control samples were labeled at either 1 or 53

[GdnCl]	3M	4M	5M	6M
Donor Lifetime Position1	3.2 ± 0.1	3.1 ± 0.0	3.1 ± 0.0	3.1 ± 0.0
Donor Lifetime Position53	3.2 ± 0.1	3.2 ± 0.1	3.2 ± 0.1	3.1 ± 0.1
Acceptor Lifetime	1.5 ± 0.0	1.5 ± 0.0	1.5 ± 0.0	1.5 ± 0.0

Table 6: ACBP 17-86: control samples were labeled at either 17 or C-terminus

GdnCl/M	2	2.5	3	4	5
Donor Lifetime Position 17	3.2 ± 0.0	3.1 ± 0.0	3.1 ± 0.0	3.1 ± 0.0	3.1 ± 0.0
Donor Lifetime C	3.1 ± 0.0	3.0 ± 0.0	3.0 ± 0.0	3.0 ± 0.0	3.0 ± 0.0
Acceptor Lifetime	1.5 ± 0.0	1.5 ± 0.0	1.5 ± 0.1	1.5 ± 0.1	1.5 ± 0.1

Note that twice measurements yielded trivial variation

In the statistically and sequentially labeled CI2 and ACBP, there is a mixture of proteins with *D* at the first site and *A* at the second site and proteins with *D* and *A* switched. The above fluorescence lifetime

controls show that this did not affect the photophysics significantly. At high denaturant concentrations (6 M GdnCl), the ΔE for the 1-53 CI2 mutant labeled with Alexa 532 and Alexa 647 is close to the Gaussian chain limit: $\langle E \rangle = 0.38 \pm 0.01$ and $\Delta E = .31 \pm .01$. Using a rise per amino acid of 0.38 nm for CI2 with 1-53 labeling, *L*=20.1 nm. Between 5M and 3.5 M GdnCl, the extracted l_P drops from $l_P = 1.4 \pm 0.1$ nm to $l_P = 0.8 \pm 0.1$ nm (comparing $\langle E \rangle$ and ΔE to simulations). For ACBP with 17-86 labeling, *L*=26.6 nm. Between 5M and 2 M GdnCl, l_P drops from $l_P = 1.3 \pm 0.1$ nm to $l_P = 0.6 \pm 0.1$ nm.

As a control, we performed measurements on a 1-40 mutant from a previous study(13) (kindly provided by Ashok Deniz) which was labeled with the donor at position 1 and the acceptor at position 40. Keeping in mind the change in R_0 (for TMR-Cy5 *D-A* pair) and that the *D-A* distance is shorter, $\langle E \rangle = 0.61 \pm 0.02$ and $\Delta E = .29 \pm .01$ (5M GdnCl). The value for ΔE is close to the Gaussian chain limit, just as for the 1-53 CI2, providing further evidence that the above labeling scheme does not explain the observed ΔE.

Triplet States of the Acceptor. One potential artifact could arise from triplet states of the acceptor. If the acceptor is in a triplet state, the donor may emit as if it were in the absence of the acceptor. This would lead to multiple exponential decays of the donor even if FRET efficiency *E* is constant. For example, consider a system where *E*=0.9, and the acceptor is in the triplet state 10% of the time. For every 10 long-lifetime photons the donor emits while the acceptor is in the triplet state, there are 9 short-lifetime photons emitted when the acceptor is not in the triplet state. This would lead to strongly multi-exponential decays.

However, for our high *E* samples (8 and 13 bp separation for dsDNA), we don't see any evidence for fluorescence with the intrinsic donor lifetime. This is consistent with recent findings that the donor remains quenched while the acceptor is in the triplet state (14).

Sample Preparation and Characterization

Protein expression and purification. *Protein expression*: A plasmid for recombinant expression of a truncated 64-residue residue double mutant (E26A/K53R) of Chymotrypsin inhibitor 2 (CI2), obtained by deletion of the first, unstructured 19 amino acids residues and replacement of Leu20 with a new starting Met was a gift from Dr. Daniel Koshland (UC Berkeley, CA). This truncated and mutated protein sequence has been shown to retain the complete structure and function of full-length CI2 and is referred to as wildtype hereafter(15). A plasmid for the expression of the 86-residue Acyl-CoA binding

protein (ACBP) was kindly provided by Dr. Kaare Teilum (University of Copenhagen, Denmark). Pairs of Cysteines were introduced into the wildtype sequences of CI2 and ACBP by site-directed mutagenesis to provide functional groups for specific conjugation with a donor-acceptor FRET-pair. For CI2, Cys were engineered between the initiation Met (residue 1 of wildtype CI2) and Lys 2, and at position 53 (loop connecting β-strand 4 and 5). In the case of ACBP, Cys were placed at positions 17 (loop connecting helix 1 and helix 2) and at the C-terminus (helix 4). Protein expression and purification of the double-Cys variants of CI2 and ACBP was performed as described for wildtype CI2 (15). Pure protein was stored at -80 °C until use. Immediately before labeling, a 1/10 volume of a 100 mM DTT-stock solution was added to the protein solution, followed by incubation for 1 h at 25 °C to reduce any disulfide bonds formed during protein storage. The protein solution was then passed through a HighLoad 16/60 Superdex 75 size exclusion column, equilibrated in buffer A (20 mM sodium phosphate, 100 mM sodium chloride, pH 7.0). Peak fractions containing monomeric protein were pooled and immediately used for labeling.

Protein labeling: Dye labeling of freshly reactivated CI2 or ACBP was carried out at 25 °C in buffer A (20 mM sodium phosphate, 100 mM sodium chloride, pH 7.0) by reacting a stoichometric amount of Alexa Fluor 647 maleimide (A647, acceptor fluorophore, C2-linker) with the protein. After 4 h incubation in the dark, unreacted dye was removed by passing the protein solution twice through a PD10 desalting column, equilibrated in buffer B (10 mM Tris, pH 8.0). Singly-labeled protein was purified from minor amounts of non-labeled or doubly-labeled protein on a Mono Q HR5/5 ion-exchange column (Amersham Pharmacia), equilibrated in buffer B, using a linear gradient in sodium chloride. Fractions containing singly-labeled protein were pooled, concentrated and passed through a PD 10 desalting column, equilibrated in buffer A. A ten-fold excess of Alexa Fluor 532 maleimide (A532, donor fluorophore, C5-linker) was added to the protein solution, followed by incubation for 4 h at 25 °C in the dark. Unreacted dye was removed by passing the protein solution twice through a PD10 desalting column, equilibrated in buffer B (10 mM Tris, pH 8.0), and doubly-labeled protein was again purified from singly labeled protein by Mono Q ion-exchange chromatography. Fractions containing double-labeled protein were pooled, concentrated, passed through a desalting column, equilibrated in buffer C (20 mM sodium phosphate, pH 6.3) (CI2) or buffer D (20 mM sodium acetate, pH 5.2) (ACBP) and stored at 4 °C in the dark until use.

Ensemble equilibrium denaturation experiments: Stability measurements were performed by mixing purified D/A-labeled protein (CI2 in buffer C, ACBP in buffer D) with increasing amounts of chaotrope (0-6 M GdnCl, prepared in buffer C or buffer D). Denaturant concentrations were determined

refractometrically (16). The thermodynamic stability of unlabeled protein was determined by monitoring the increase in tryptophane fluorescence emission fluorescence intensity upon unfolding. Protein concentrations of 5 μM were employed. After incubation for 4 h at 25°C, fluorescence emission spectra were recorded from 310 nm to 420 nm (excitation at 295 nm). The stability of the D/A-labeled protein was determined in buffer C (CI2) or D (ACBP) (containing 100 μg/ml bovine serum albumine (BSA) to minimize adsorption of the protein to the cuvette wall) by recording acceptor fluorescence emission spectra from 650 nm to 740 nm after excitation at 532 nm (A-emission due to FRET) and 630 nm (direct excitation of A) as a function of denaturant concentration. A protein concentration of 10 nM was used. Unfolding transitions were fitted to a standard two-state unfolding model (Santoro and Bolen, Biochemistry, 1988). Unfolding transitions of labeled and non-labeled protein, normalized to the fraction of unfolded protein, are essentially superimposable, ruling out a significant perturbation of the energy landscape of CI2 or ACBP upon dye-labeling (Figure 18):

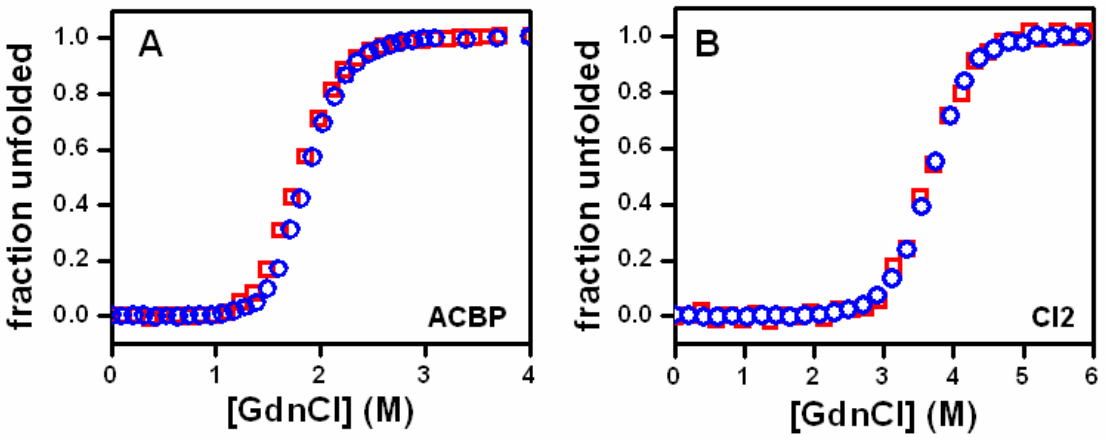

Fig. 18. Equilibrium unfolding transitions, normalized to the fraction of unfolded protein, for non-labeled (open blue circles) and labeled (open red squares) ACBP (A) and CI2 (B).

ssDNA and dsDNA Preparation. *dsDNA:* Oligodeoxyribonucleotides were prepared by automated synthesis (17), labeled, and hybridized to form *D-A* double-stranded DNA (dsDNA) fragments. For the set of 5 DNA fragments the top-strand sequence was 5'-TAAATCTAAAGTAACATAAGGTAACATAACGGTAAGTCCA-3', with amino-C6-dT residues (Glen Research, Sterling, VA) at position 1 of the top strand, and at each of positions 8, 13, 18, 23, or 28 of the bottom strands (positions underlined in the top-strand sequence shown above). Oligodeoxyribonucleotides were HPLC-purified, labeled with *N*-hydroxy-succinimidyl esters of carboxytetramethylrhodamine (TMR) or Alexa 647 (Molecular Probes, Eugene, OR) using manufacturer's instructions, and HPLC-purified. We incorporated TMR (FRET donor) at position 1 of the top strand, and Alexa 647 (FRET acceptor) at each of five distinct positions in the bottom strand; the acceptor was incorporated within the same 3-bp sequence (TAA) to eliminate any changes in

fluorescence properties due to change in local environment. dsDNA was formed by hybridization of top and bottom strands in 40 mM Tris-HCl pH 8, 500 mM NaCl after heating for 2 min at 95°C and cooling to 25°C overnight; we used 50% molar excess of *D*-labeled top strand to ensure complete hybridization of *A*-labeled bottom strands.

For the set of internally labeled DNA fragments the top-strand sequence was 5'-TTCTTCACAAACCAGTCCAAACTATCACAAACTTA-3', with amino-C6-dT residues at position 5 of the top strand, and at each of positions 10, 20, or 30 of the bottom strands (positions underlined in the top-strand sequence shown above). These DNA fragments were prepared the same as described above, but with Alexa 647 at position 5 on the top strand, and TMR at each of the three distinct positions in the bottom strand.

ssDNA: DNA fragments $(dT)_{30}$ were prepared by automated total synthesis. Trityl-ON DNA fragments were HPLC-purified using a C2/C18 µRPC column (APB, Piscataway, NJ) on an ÄKTA Purifier (APB), labeled with amine-reactive TMR and Alexa647. Samples were later diluted in SMF buffer (20mM TRIS-pH8, 1mM mercaptoethylamine [MEA], 100µM EDTA, 100µg/mL bovine serum albumin [BSA] and NaCl ranging from 1mM to 2M).

Data Acquisition Conditions. All experimental data were acquired using nsALEX setup described in figure 6 at room temperature. All samples were prepared at 50 pM concentrations of sample. A 100x oil-immersion objective with 1.40 numerical aperture was used to place the focal point in solution (20 µm from the surface), and a 100 µm pinhole was placed at the image plane to reject out-of-focus light. The excitation intensities were 120 µW at 532 nm, and 30-60 µW at 635 nm. Photon streams were detected by avalanche photodiodes, and recorded using a TCSPC plug-in board (SPC-630, Becker and Hickl GmBH). All data points are averages of two or three independent experiments, error bars are standard error of the mean.

1. Laurence, T. A., Kapanidis, A. N., Kong, X. X., Chemla, D. S. & Weiss, S. (2004) *J. Phys. Chem. B* **108,** 3051-3067.
2. Fries, J. R., Brand, L., Eggeling, C., Kollner, M. & Seidel, C. A. M. (1998) *J. Phys. Chem. A* **102,** 6601-6613.
3. Barzykin, A., Seki, K. & Tachiya, M. (2002) *J. Chem. Phys.* **117,** 1377-1384.
4. Srinivas, G., Yethiraj, A. & Bagchi, B. (2001) *J. Chem. Phys.* **114,** 9170-9178.
5. Dale, R. E., Eisinger, J. & Blumberg, W. E. (1979) *Biophys. J.* **26,** 161-93.
6. dos Remedios, C. G. & Moens, P. D. (1995) *J. Struct. Biol.* **115,** 175-85.
7. Ermak, D. L. & Mccammon, J. A. (1978) *J. Chem. Phys.* **69,** 1352-1360.
8. Haas, E., Katchalskikatzir, E. & Steinberg, I. Z. (1978) *Biopolymers* **17,** 11-31.

9. Rachofsky, E. L., Osman, R. & Ross, J. B. A. (2001) *Biochemistry* **40,** 946-956.

10. Doi, M. & Edwards, S. F. (1986) *The theory of polymer dynamics* (Clarendon, Oxford Univ. Press, Oxford).

11. Lapidus, L. J., Steinbach, P. J., Eaton, W. A., Szabo, A. & Hofrichter, J. (2002) *J. Phys. Chem. B* **106,** 11628-11640.

12. Wang, X. & Nau, W. M. (2004) *J. Am. Chem. Soc.* **126,** 808-13.

13. Deniz, A. A., Laurence, T. A., Beligere, G. S., Dahan, M., Martin, A. B., Chemla, D. S., Dawson, P. E., Schultz, P. G. & Weiss, S. (2000) *Proc. Natl. Acad. Sci. USA* **97,** 5179-84.

14. Tinnefeld, P., Buschmann, V., Weston, K. & Sauer, M. (2003) *J. Phys. Chem. A* **107,** 323-327.

15. Radisky, E. S. & Koshland, D. E., Jr. (2002) *Proc. Natl. Acad. Sci. USA* **99,** 10316-21.

16. Pace, C. N. (1986) *Methods Enzymol.* **131,** 266-280.

17. Kapanidis, A. N., Lee, N. K., Laurence, T. A., Doose, S., Margeat, E. & Weiss, S. (2004) *Proc. Natl. Acad. Sci. USA* **101,** 8936-41.